Sources of light-charged-particle emission in the reaction 480 MeV ^{56}Fe+^{nat}Ag

G. F. Peaslee,* N. N. Ajitanand,† John M. Alexander, D. Guerreau,‡
Roy Lacey,§ and L. C. Vaz
Department of Chemistry, State University of New York at Stony Brook, Stony Brook, New York 11794

Morton Kaplan, M. Kildir,** and D. J. Moses
Department of Chemistry, Carnegie-Mellon University, Pittsburgh, Pennsylvania 15213

D. Logan†† and M. S. Zisman
Lawrence Berkeley Laboratory, Berkeley, California 94720
(Received 19 May 1988)

Inclusive and exclusive measurements of light-charged particles (^{1,2,3}H,^{4}He) and heavy fragments have been made for the reaction 480 MeV ^{56}Fe+^{nat}Ag. The backward hemisphere emission of ^{4}He and ^{1}H in coincidence with a heavy fragment can be well described by evaporative emission from a combination of three sources: the detected fragment, the undetected fragment, and the composite system prior to scission. Multiplicities for each of these sources are determined for two coincident fragment groups: a fusion-fission-like group and a deeply-inelastic-reaction group. These multiplicities have also been studied at two angles for the trigger fragment ($\theta_{TR}=26°$ and 50°). For $\theta_{TR}=26°$ the multiplicity of the light-charged particles (^{1}H or ^{4}He) emitted from the composite nuclear system (i.e., prior to scission) is $\approx\frac{2}{3}$ for the fusion-fission-like fragments, compared to $\approx\frac{1}{3}$ for the deeply inelastic reactions. This decrease implies that the deeply inelastic reactions occur in $\approx\frac{1}{2}$ the time required for fission reactions. For the deeply inelastic reactions, these multiplicities change with trigger angle. This result also suggests that the lifetime of the composite system exerts some control on the extent of evaporative particle emission. Energy and angular distributions of the coincident light particles suggest extensive emission from a strongly deformed composite system, such as that of a system en route to scission. Low-energy ^{4}He particles at forward angles, which cannot be attributed to evaporation, exhibit a dependence on the angle with respect to the scission axis. This result is attributed to emission that occurs very near to the instant of scission. High-energy ^{4}He particles at forward angles are emitted prior to thermalization; they do not depend on the angle with respect to the scission axis.

I. INTRODUCTION

Light-charged-particle evaporation in heavy-ion reactions has emerged as a very useful tool for probing the dynamics of nuclear reactions. For heavy projectiles at energies (E/A) less than 20 MeV/nucleon, it has been shown that evaporative processes are prominent compared to preequilibrium processes.[1] Light-charged-particle evaporation has been found in coincidence with evaporation residues[2] produced in central collisions as well as with fusion-fission, and deeply inelastic reactions[3–6] that result from more peripheral collisions. It is interesting to note that, for each of these reaction mechanisms, evaporative particles have been observed to arise from the composite nucleus prior to scission (see, for example, Refs. 1, 3, and 6–15). In addition, particle evaporation occurs from one or both heavy fragments after scission[6] and even near to the moment of scission.[16]

Since particle evaporation seems to accompany many types of nuclear reactions, and indeed all stages of any particular reaction, it is natural to try to use this phenomenon as a probe of the individual reaction mechanisms, as well as the different stages of the reactions. To this end, we have chosen the reaction 480 MeV ^{56}Fe + ^{nat}Ag for a study of particles in coincidence with the three reaction classes above; the results give insights into the different stages of each reaction. This reaction has been shown to give a broad distribution of heavy fragments,[17] as well as a bountiful yield of light-charged particles.[10] Measurements of the energy and angular distributions of the evaporative particles, together with the well-developed statistical model of evaporation,[18,19] provide an interesting probe of the properties of the emitting nuclei. One can expect this probe to be sensitive to the temperature, spin, and deformation of the emitter, and perhaps even its lifetime. From the statistical evaporation theory, one knows that certain angular symmetries must be obeyed if thermal equilibrium is indeed achieved. Perturbations of these symmetries (shadows,[12,16] for example) can also shed light on the nature of the emitter.

In this study of ^{56}Fe + ^{nat}Ag we present inclusive data for both the fragments (Sec. III) and the particles (Sec. IV), and we use these measurements (along with others in the literature) to gain an overall view of the various reaction mechanisms. The most informative applications of the light-charged-particle probe arise from the require-

ment of a coincidence trigger. In Sec. V we present results for ^{4}He and ^{1}H in coincidence with heavy fragments separated by atomic number (Z). This coincidence trigger was used to emphasize two different reaction mechanisms: the deeply inelastic reaction (DIR) and the fusion-fission-like breakup (FF). By use of a reaction simulation code along with these data, we determine the overall abundance of prescission and postscission emission, and we obtain information about the lifetime of the composite nucleus. In Sec. VI we show spectra for ^{4}He at forward angles, also in coincidence with Z separated fragments. These results provide distinctions between prethermalization emission and near-scission emission of ^{4}He. In Sec. VII we examine the input parameters used in the reaction simulations. We compare their values to those expected for a classical spherical emitter in an effort to gain insight into the possible shapes of the various emitters. The detailed results of our particle-particle coincidence study[20] (and related deductions concerning associations with evaporation residues) will be published elsewhere.

II. EXPERIMENTAL METHOD

A beam of ^{56}Fe of 8.5 MeV/nucleon was obtained from the Lawrence Berkeley Laboratory Super-HILAC. After passing through circular and four-jaw collimators (≈ 3 mm)^2 the beam traversed a self-supporting ^{nat}Ag target foil of 904 μg/cm^2 and was collected in a Faraday cup. Heavy fragments, ranging in atomic number from $Z=7$ to 45 were detected in gas ionization telescopes (GT's) of approximately 4 msr solid angle.[21] The GT's were positioned for coincidence measurements at two angles: 26° (near the grazing angle of 23.5°) and 50° (well away from the grazing angle). However, for singles measurements the GT's were also placed at additional angles to determine angular distributions of the fragments. Light-charged particles were detected in four, three-member, solid-state telescopes (SST's), as well as in two ionization telescopes or "wedge" detectors (gas ΔE and solid-state E). Each of these wedge detectors consisted of five stopping detectors in an arc, sharing a common gas ΔE section.[22] One of the side-angle SST's was mounted out of plane (60°), as was one of the wedge detectors (0° to 40° out of plane).

Fourteen in-plane detector angles and ten out-of-plane detector angles were used as shown in Fig. 1 to record light-charged-particle coincidences. For simplicity, we present coincidence data from only certain detector angles, such as those especially indicated in Fig. 1. The other detectors provided corroborating data, but the essential results can be seen clearly from the chosen subset. Fragment-particle coincidences were recorded, as well as particle-particle coincidences between the SST's and the wedge detectors. Standard Nuclear Instrumentation Modules (NIM) electronics were used to process the signals from the detectors; analog signals were digitized and written on magnetic tape by a Modcomp IV computer for subsequent off-line analysis. We report here on singles measurements for light-charged particles and fragments and coincidence measurements between fragments and particles. Singles measurements were also recorded with

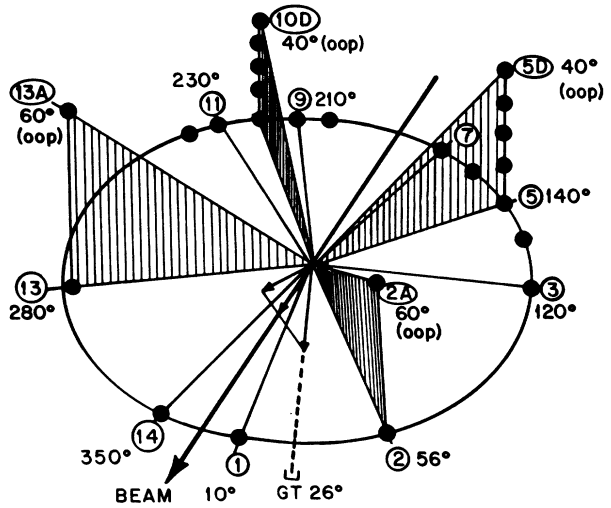

FIG. 1. Schematic diagram of the detector setup for the reaction 480 MeV ^{56}Fe + ^{nat}Ag. In this configuration, fragments were detected in a gas-ionization telescope (GT) at $\theta_{TR}=26°$. For a second configuration θ_{TR} was set to 310° or $-50°$. Light-charged particles were detected at the positions indicated by closed circles. Note that only some of the representative detectors have been numbered for the sake of clarity. Detectors 1, 2, 2A, 13, 13A, and 14 were solid-state telescopes (SST's), the rest were ionization chambers ("wedge" detectors). This diagram takes advantage of the symmetry associated with two actual fragment telescopes (at +26° and −26°). Hence each particle detector is shown at two angles. The detector setup without use of the symmetry conditions is shown in Fig. 1 of Ref. 6 (after identical rotations of the two GT's and side-angle SST's).

gold and carbon targets of known thickness to determine the Ag target thickness and to allow for a correction for carbon impurities that deposit on the target. Energy calibrations for each silicon detector were obtained with ThB sources, and a ^{252}Cf source was used to measure the pulse-height defect of the heavy-fragment detectors.[23] Solid angles were determined from a calibrated ^{241}Am source as well as from geometric measurements.

III. FRAGMENT SINGLES

Heavy-fragment singles cross sections were measured at several angles between 23° and 55°. Figure 2 compares ΔE-E maps (26° and 50°) to Z-E maps as obtained by transformation with a standard algorithm.[24] Our atomic number (Z) resolution is ≈ 3 units (FWHM). The ability to identify heavier fragments deteriorates rapidly at the more backward angles. At 26° we could classify three fragment groups by Z, and at 50° we could still classify two such fragment groups. Overlaid on Fig. 2 are the Z gates we have used for the fragment coincidence studies described below.

The horizontal band of fragments [Figs. 2(b) and 2(d)], visible at both angles, corresponds to a projectile-like-fragment (PLF) peak of $Z \approx 26$ that persists at all measured angles and over a large range of fragment energies. For strongly damped reactions with fragment energy less

than 300 MeV, this peak is mainly attributed to the class of reactions usually called deeply inelastic reactions DIR (not distinguished from quasifission). The horizontal tail of the PLF locus extending below 100 MeV is ascribed to slit scattering of the beam; its low intensity in encouraging. Figure 3 shows charge distributions of the strongly damped fragments ($100 < E_{lab} < 300$ MeV) at 26° and ($70 < E_{lab} < 300$ MeV) at 50°. The PLF peak at $Z \approx 26$ can be seen at both angles. There is no experimental technique to separate completely the fusion-fission fragments from these DIR fragments. We have simply divided the observed cross section into two Z groups at each angle: one group of dominance for fissionlike fragments ($29 < Z < 37$) and another for which the DIR peak dominates ($21 < Z < 29$). For the data at 50° we make a Gaussian fit (as shown in Fig. 3) and use it as described below. At 26° it was possible to isolate a third group of fissionlike fragments ($37 < Z < 45$) with Z values greater than that for symmetric breakup.

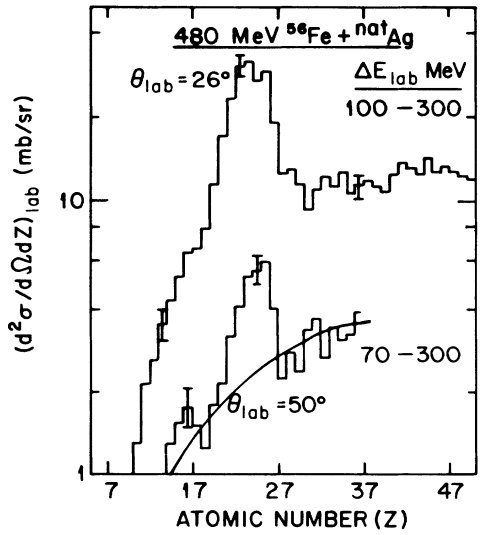

FIG. 3. Inclusive cross section vs atomic number for the fragment trigger angles 26° and 50°. Note the DIR peak for $Z = 26$ at both angles. For the 50° data, a Gaussian has been fit to the FF component.

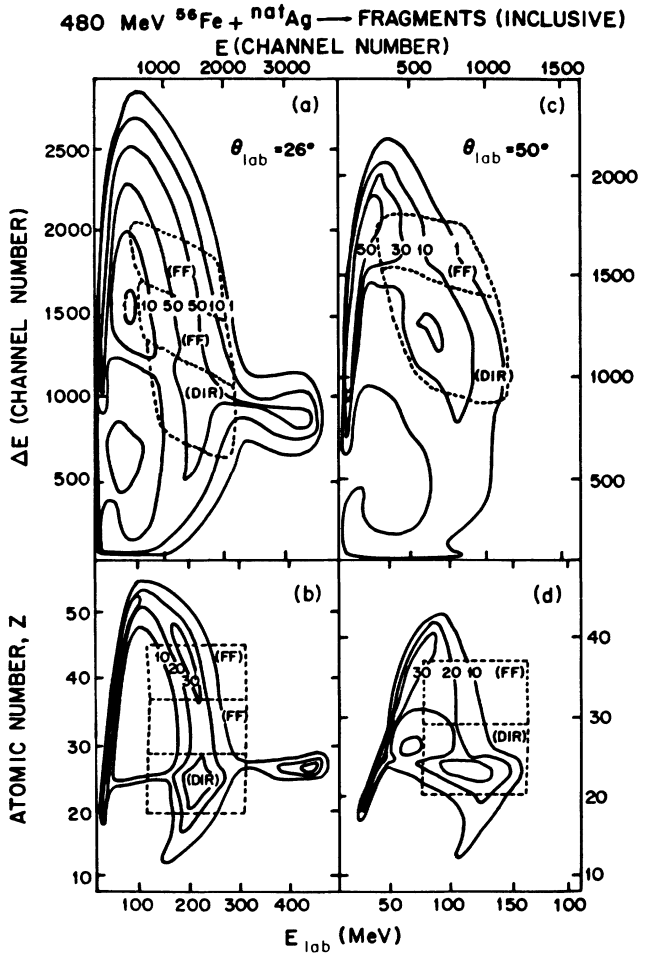

FIG. 2. Contour maps of the response for heavy fragments in the GT's. Detection angle $\theta_{lab} = 26°$ is on the left (a) and (b), and detection angle $\theta_{lab} = 50°$ is on the right (c) and (d). On the top (a) and (c) is the raw ΔE vs E in channel number, and on the bottom (b) and (d) the same data have been translated into atomic number, Z vs E in MeV. Overlaid on the maps are outlines of the gating conditions used to separate the DIR components ($21 < Z < 29$) from the FF components ($29 < Z < 37$ and $37 < Z < 45$).

For strongly damped fragments with ($E_{lab} < 300$ MeV and $10 < Z < 37$), the inclusive cross sections are plotted in Fig. 4 as a function of the average c.m. angle. Only the fragments of Z less than that for symmetric breakup were included. To avoid misidentification of Z, a low-energy cutoff was used between 50 and 100 MeV (depending on the angle). The angular distribution seems to be significantly more forward peaked than a $1/\sin\theta_{c.m.}$ dis-

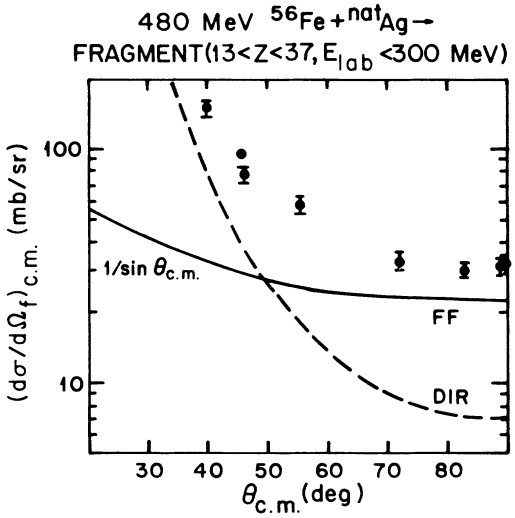

FIG. 4. Angular distribution of inclusive heavy fragments in the c.m. Fragments were divided into small Z slices between $Z = 13$ and $Z = 37$, converted into an average c.m. angle, and then summed. The solid curve is for $1/\sin\theta_{c.m.}$, and it was normalized to the symmetric breakup component (FF) at $\theta_{c.m.} \approx 90°$. The dashed curve (DIR) is obtained by subtracting this component from the data.

tribution which is also shown. It is interesting to note that both the fissionlike fragments ($29 < Z < 37$) and the DIR fragments ($21 < Z < 29$) appear to show this steep angular distribution in the first quadrant. Such steep angular distributions have previously been observed for this reaction,[17] as well as for other reactions.[25] If a completely equilibrated compound nucleus is formed and if the system rotates many times, then it will lose all forward-backward asymmetry; in this case the limiting angular distribution is $\approx 1/\sin\theta_{\text{c.m.}}$. These requirements are apparently not satisfied by the more strongly forward-peaked fragments. To examine these fragments in more detail, we have simulated the energy spectra of the Z group 29–37 both at 26° and at 50°, using standard distribution functions for binary fission (described in Ref. 26). We find that the 26° data require an average total kinetic energy (TKE) value that is ≈10% higher than that required for the 50° data. This implies that the fragments in the $29 < Z < 37$ group, detected at 26°, which we have labeled as fusion-fission-like events, must include a component of higher TKE that is not completely damped. From other studies in this mass and energy regime[27,28] it is reasonable to expect some "fuzziness" in the distinction between FF and DIR groups, if they are based only on Z selection. This notion weakens the distinction between the "FF and DIR gates" used for our particle coincidence studies, but by no means eliminates it.

To integrate the fragment cross sections, we have divided the measured values, close to 90° in the c.m., into FF and DIR contributions. At these angles (for the 50° data, for example), the projectilelike peak has diminished, and we estimate the fusion-fission yield by a Gaussian fit to the Z distribution, as shown in Fig. 3. These best estimates for the FF contributions for $70° < \theta_{\text{c.m.}} < 100°$ are then used to normalize the solid curve ($1/\sin\theta_{\text{c.m.}}$) shown in Fig. 4. From time-of-flight studies of similar systems[28] and from the systematics of fission angular distributions[29] we expect this FF component to exhibit a $1/\sin\theta_{c.m.}$ distribution; thus we have used this form to describe and integrate the FF contribution. By subtracting this component from the measured cross sections at c.m. angles less than 70°, we deduce the angular distribution for DIR shown in Fig. 4. Integration of the $1/\sin\theta_{\text{c.m.}}$ curve gives us an estimate of 454±150 mb for the fusion fission. Numerical integration of the dashed curve gives 819±300 mb; we assign this value to the DIR component. The large error bars reflect our estimate of the uncertainty in this general procedure. From the results of Ref. 28 for the reactions $^{56}\text{Fe} + ^{120,122}\text{Sn}$, we have estimated the evaporation-residue (ER) cross section to be 240±75 mb for $^{56}\text{Fe} + ^{\text{nat}}\text{Ag}$.

In the sharp-cutoff approximation, these values lead to spin-zone divisions shown in Fig. 5 and summarized in Table I. A large portion of the total reaction cross section, as calculated in Ref. 30, seems to be comprised of quasielastic reactions. Near the grazing angle we do observe many fragments with lab energy greater than 300 MeV, but, since relatively little kinetic energy is dissipated in these reactions, charged-particle coincidences were found to be be minimal in the backward hemisphere. The l values in Table I have rather large error bars because

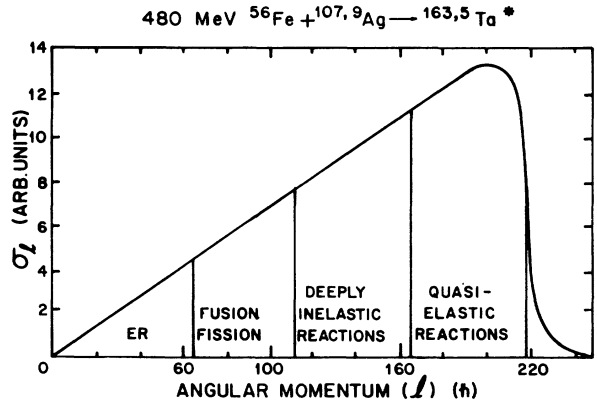

FIG. 5. Schematic diagram of the reaction cross section as a function of entrance channel angular momentum l. The values shown were deduced from the measured fragment cross sections and systematics. (See Table I).

they are dependent on an ER cross section deduced from systematics, as well as the division of fragment cross sections detailed above. Even with these uncertainties, it is apparent that this reaction can produce very hot, high-spin composite systems that exist for some fraction of a rotation, or sometimes even several rotations, before binary breakup occurs. In this study, we use light-charged-particle spectra to reflect the extent of energy equilibration and to probe the early existence of the nuclear-collision complex.

IV. PARTICLE SINGLES

Light-charged particles (^{1,2,3}H and ^{4}He) were measured in the SST's and ^{4}He was also measured in the wedge detectors. (The isotopes of ^{1}H were also recorded in the

TABLE I. 480 MeV $^{56}\text{Fe} + ^{107,109}\text{Ag} \rightarrow ^{163,165}\text{Ta}^*$ ($E^* \approx 211$ MeV): Inclusive cross sections and spin zones.

Heavy fragment groups and associated spin limits	
σ_{Reaction} (mb)[a]	2694
l_{max} ($\hbar$)	218
$\sigma_{\text{FF}} + \sigma_{\text{DIR}}$ (mb)	1273±330
l_{DIR} ($\hbar$)	163±20
σ_{FF} (mb)	454±150
l_{crit} ($\hbar$)	110±13
σ_{ER} (mb)[b]	240±75
l_{ER} ($\hbar$)	64±8
Light-charged particles from evaporation[c]	
σ (^{4}He) (mb)	1790±125
σ (^{3}H) (mb)	80±20
σ (^{2}H) (mb)	260±50
σ (^{1}H) (mb)	3205±250

[a]From Ref. 30.
[b]Estimated from Ref. 28.
[c]$\sigma = 4\pi \int_{\pi/2}^{\pi} (d\sigma/d\Omega)\sin\theta_{\text{c.m.}}\, d\theta_{\text{c.m.}}$ The forward-peaked components are not included in the integration.

wedge detectors, but the ΔE resolution and punch through of the E detector made it impossible to differentiate ^{1,2,3}H or to measure the total energy.) The angular distribution of ^{4}He is given in Fig. 6; numerical integration using the backward-hemisphere data yields a cross section of 1790±125 mb. It is interesting to note that the observed anisotropy for ^{4}He (in the backward hemisphere) is very similar to that measured for the reaction 337 MeV ^{40}Ar + ^{nat}Ag.[3] For that reaction, complete angular distributions were also measured for ^{1,2,3}H as well. We use the angular distributions of ^{1}H, ^{2}H, and ^{3}H from that study (they are nearly isotropic) along with our data for $\theta_{lab} \approx 60°$ to get integrated cross sections of 80±20 mb for ^{3}H, 260±50 mb for ^{2}H, and 3205±250 mb for ^{1}H. Note that for the 1513-mb cross section for the strongly damped reactions (240 mb ER + 454 mb FF + 819 mb DIR), we observe roughly 1.2 ^{4}He particles and 2.1 ^{1}H particles per reaction. (Very few coincident particles were observed for the weakly damped fragments of $E_{lab} > 300$ MeV.)

In Fig. 7 we present a representative display of ^{4}He singles spectra, plotted in the center-of-mass frame. We note the similarity of spectral shape at all but the most forward angles. To give further detail, we show in Fig. 8 a contour map of the invariant cross sections. At the most backward angles there is a significant departure from circles centered about the c.m. velocity. This could arise from strong spin effects on a composite nuclear emitter or from evaporative sources not traveling with average velocity equal to that of the c.m. (e.g., from targetlike fragment emission in DIR). All of the forward-angle spectra show additional contributions to the cross section due to preequilibrium process (not plotted in Fig. 8 but discussed below). In Fig. 9 we show angular distributions of the alpha particles as a function of their channel energy. This plot shows that the high-energy α's exhibit the strongest backward peaking, as would be expected for a spin-driven anisotropy from a composite nuclear emitter. This feature can also be expected for emission from fission fragments.

All of these data suggest that there might be a significant amount of emission from the composite nucleus. However, as we have noted, there are other reaction mechanisms that can also contribute to the production of light-charged particles. In the next section we use fragment-particle coincidences along with a reaction simulation code to determine the division of particles according to source, i.e., between the composite nuclear system and the fully accelerated fragments.

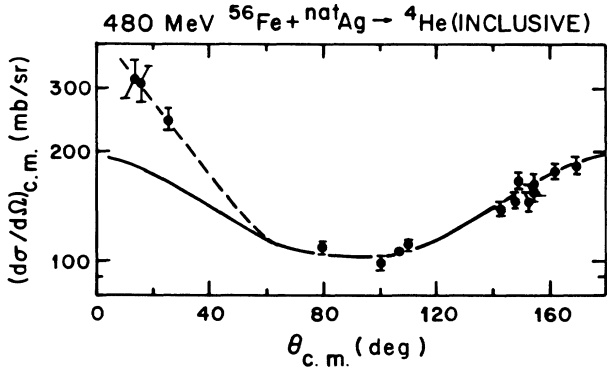

FIG. 6. Measured c.m. angular distribution for inclusive ^{4}He. The solid curve is a symmetric fit to the backward hemisphere data. Integration of this component gives 1790±125 mb.

V. FRAGMENT-PARTICLE COINCIDENCES AND REACTION SIMULATION ANALYSIS

Nuclear evaporation is a well-formulated, statistically determined mechanism for producing light-charged parti-

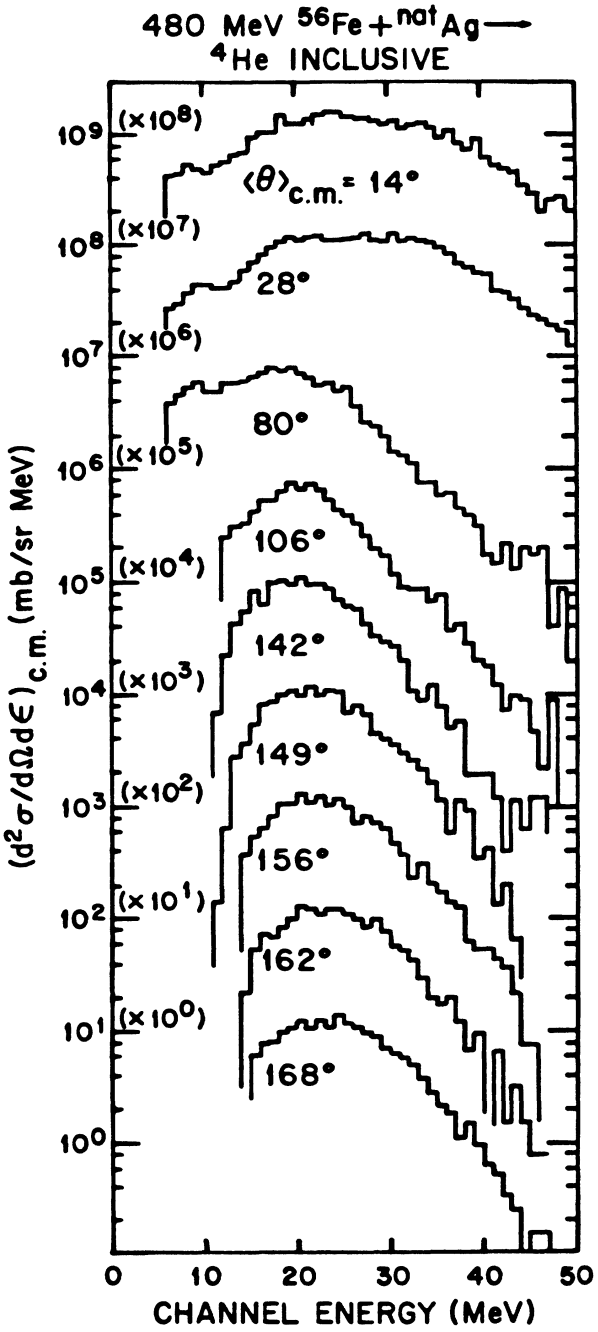

FIG. 7. Typical c.m. spectra for inclusive ^{4}He at several angles. Note the similarity in spectral shape for the backward-angle detectors.

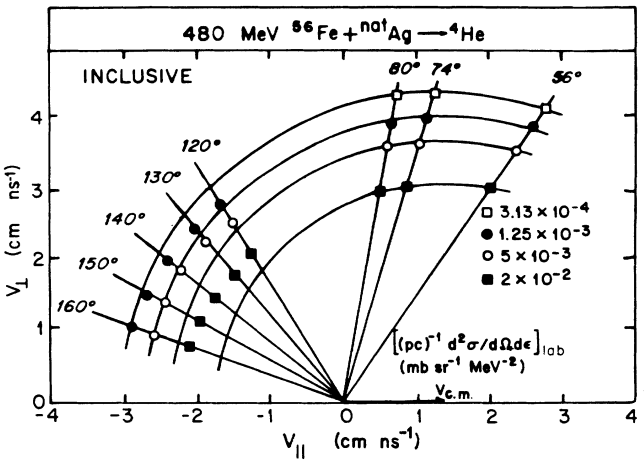

FIG. 8. Invariant cross-section contour map for inclusive ^{4}He. Only the high-velocity data for the backward-angle detectors are plotted. Circles are drawn concentrically around $V_{c.m.}$.

cles (reviewed in Refs. 18, 19 and 31). Such evaporative emission exhibits cylindrical symmetry about the spin axis of the emitter, and is controlled by the transmission coefficient T_l for each exit-channel l wave and the level density $[\rho(E^*,J)]$ of the daughter nucleus. However, even for a single compound nucleus with a unique excitation energy (E^*) and spin (J_0), it is difficult to write an exact analytic equation for the energy spectra of the evaporated particles.[1] We have developed a Monte Carlo reaction simulation code GANES to describe these spectra and angular distributions from evaporation theory, along with the kinematic shifts associated with the velocity spectra of the emitters (e.g., the fission of DIR fragments and the composite nuclei). A complete description of the program may be found in Ref. 26. The basic objective of this reaction simulation is to calculate the laboratory spectra for evaporative emission from each possible emitting nucleus. Briefly, the program performs the repetitive addition of vectors after taking into account the various physical effects that control the intrinsic evaporation spectra. Among these are barrier penetration, magnitude and orientation of the emitter spin, recoil effects, and the angular, energy, and mass distributions of the FF and DIR fragments.[17,29,32–34]

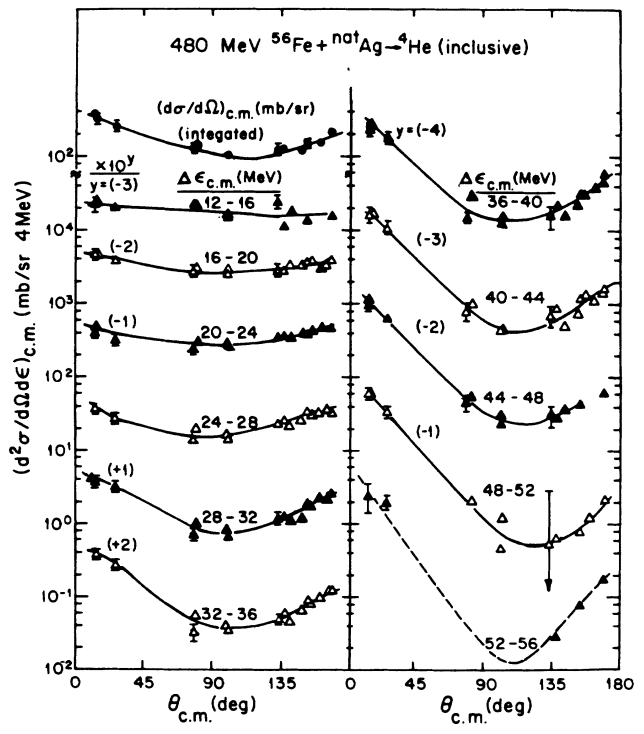

FIG. 9. Measured c.m. angular distributions of inclusive ^{4}He particles for various channel energy bins. The total inclusive ^{4}He distribution is given at the top for reference.

The inclusion of these physical ingredients results in a rather elaborate description of the particle spectra, however, the major features of the calculated spectra are often simply due to the kinematics, i.e., the vector addition of emitter and particle velocities. As a result, the selection of parameters is, in some cases, not very crucial. For example, in the ^{56}Fe + ^{nat}Ag system simulated here, the emission of particles from the fragments is dominated by the fragment velocity vectors and the associated Jacobians. By contrast, for simulation of particle evaporation from the composite system (of unique velocity), the effects of spin and excitation energy of the composite nucleus are also very important for the calculated spectra.

Figure 10 shows ^{4}He particle spectra in coincidence with one group of the fusion-fission-like fragments at 26°. Only fragments with $29 < Z < 37$ were selected for this coincidence gate. Seven representative energy spectra are displayed, circling the backward hemisphere, where evaporative processes are expected to dominate. The positions of the particle detectors are marked on the central velocity diagram, together with the velocity of the center-of-mass system and the average velocity of each fragment. The energy, mass, and angular distributions of the detected fragments have been matched in the GANES simulation, and properties of the complementary fragment vectors have been calculated from two-body kinematics, including recoil effects from particle evaporation. On the central velocity diagram, the solid and dashed curves represent the average ^{4}He emission velocity from each of three sources; one circle is large and centered on $V_{c.m.}$, representing composite nuclear emission (CE), while smaller circles are centered on each of the average fragment velocities, representing fragment emission (FE). The results of the simulation are shown as thin solid (CE) and dashed (FE) curves overlaid on the particle histograms; thick solid curves give their sum.

It can be seen immediately from the vector diagram that this particular coincidence trigger would strongly disfavor the production of ^{4}He in detector No. 3 from either of the fragments. The average velocity of ^{4}He particles from the heavier fragment barely clears the experimental threshold of the detector, which is represented by the end of the detector bar. Only the high-energy fringe of the fragment evaporation could reach this detector. However, evaporative ^{4}He from a high-Z source moving

at $V_{c.m.}$ would populate the energy region well above the threshold of the detector, close to the experimentally observed average energy of 10 MeV. Thus the high-energy side of the experimental spectrum from position No. 3 can be used to normalize the simulation for composite nuclear emission. This normalization fixes the CE contribution in every other detector, as given by the simulation. It can be seen that a major part of all the spectra can be accounted for by this composite nucleus emitter. At side angles, however, especially on the opposite side of the beam from the trigger detector, there are other components identifiable as excess cross section not accounted for by the CE simulation. Just as one detector can fix the CE component, any of the sideward angle detectors, after subtraction of the CE contribution, can fix the contribution from the respective fissionlike fragments. Once the amount is fixed from one detector, the calculated angular distribution fixes all of the FE contributions from that fragment.

Figure 10 shows our best fit to the data from these simulations of CE and FE. The parameters used in the simulation will be discussed in Sec. VII. Finally, the simulation integrates over all space (4π) (using the relative normalizations obtained here) to obtain the multiplicities of both CE and FE. The same procedure was followed (with essentially the same results) for the heavier fragments ($37 < Z < 45$) for the trigger at 26° (see Fig. 11). The experimental multiplicities for the fusion-fission-like group, as determined by this method are 0.56 for CE, 0.40 for FE, and 0.96 for their sum. These values are listed in Table II along with all the other multiplicities determined in this study. In the following paragraphs we comment in some detail on each separate determination.

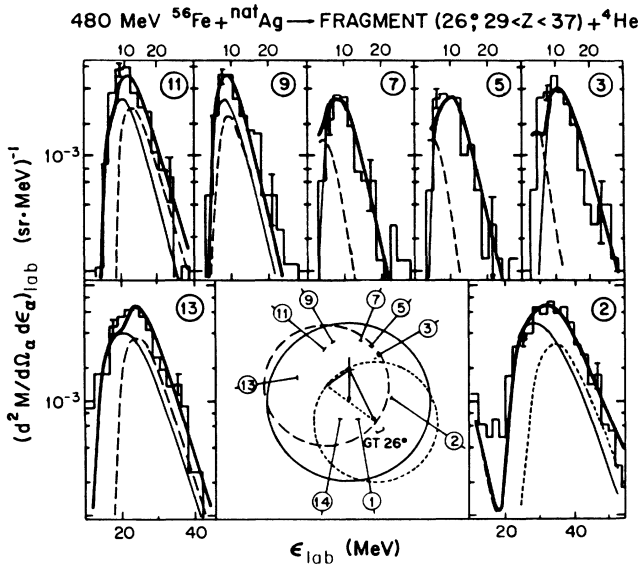

FIG. 10. Fragment-particle coincidence spectra (histograms) at several angles overlaid by reaction simulations (curves). Spectra for ^{4}He are plotted in units of differential multiplicity. The velocity diagram in the center identifies the detectors by number as in Fig. 1, and shows the average velocity for a ^{4}He particle emitted from three sources: the composite nuclear emitter (CE, thin solid line), the lighter fragment, and the heavier fragment emitters (FE, short- and long-dashed lines). This convention is also used for the calculated spectra. The summed spectrum from all three sources is represented by a thick solid line. A few error bars are also shown. Arrows in the velocity diagram represent the average measured velocity for the detected and undetected fragments and the c.m. velocity. The trigger fragments here are predominantly from fusion-fission-like reactions FF with $29 < Z < 37$. The experimental thresholds are represented by the crossbar closest to the origin for each detector.

Figure 12 shows ^{4}He spectra for coincidences with deeply inelastic reaction products. As the projectilelike fragment (PLF) is light, its velocity is large, while its complement, the targetlike fragment (TLF), has a rather small velocity vector. Again, the high-energy side of the spectrum from position No. 3 serves to fix the extent of CE contribution, as ^{4}He emitted from the fragments will be very unlikely at that angle. If one assigns a smaller CE contribution, there will be a lot of unaccounted-for cross section in most of the detectors. It would not be possible, for example, to account for the spectrum in detector No. 3 by any amount of FE alone. As mentioned in the Introduction, we have made measurements at 14 in-plane detector angles, all of which were used in this process; only seven are displayed here. In Fig. 12 it can be seen that the contribution from the fragments (FE) is as large as (if not larger than) the contribution from the composite nuclear emitter (CE). The ratio determined for this coincidence gate corresponds to an overall abundance of approximately 40% CE and 60% FE. This is a reversal of the ratio observed for the fission-fragment-like gate. The experimentally determined (or best-fit) multiplicities for the DIR gate at 26° are 0.26 for CE, 0.16 for PLF, 0.30 for TLF, and 0.72 for their sum.

We interpret the difference in CE multiplicities, from FF to DIR triggers, as mainly due to the respective lifetimes of the composite nuclear emitters. For deeply inelastic reactions detected at 26°, the amount of time avail-

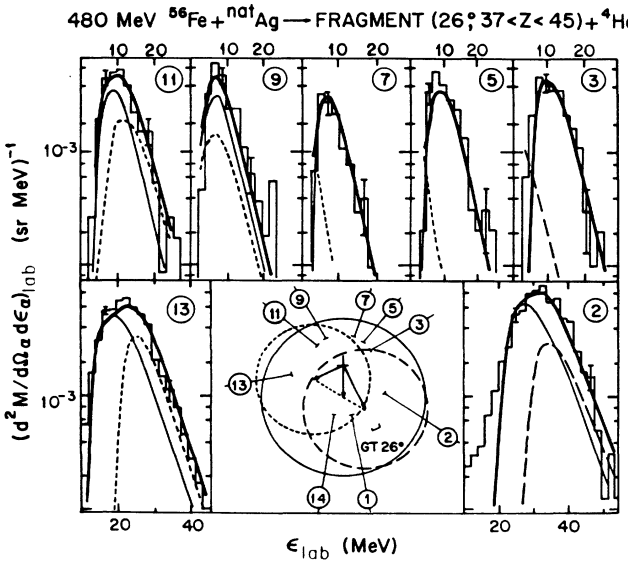

FIG. 11. Same as Fig. 10, except for FF trigger fragments of $37 < Z < 45$, $\theta_{TR} = 26°$.

TABLE II. 480 MeV $^{56}Fe + {}^{nat}Ag$: Measured cross sections and multiplicities from fragment-particle coincidences.[a,b]

	M_{CE}	M_{CE},σ (mb)	M_{FE}	$M_{FE}\sigma$ (mb)	$\sigma_{CE}+\sigma_{FE}$ (mb)
		Fragment-detection angle, $\theta_{TR}=26°$			
FF-α	0.56	254±88	0.40	182±63	436±108
DIR-α	0.26	213±68	0.16 + 0.30[c]	377±121	590±139
FF-p	0.81	368±142	1.35	613±237	981±276
DIR-p	0.35	287±105	0.45+0.86[c]	1073±392	1360±406
		Fragment-detection angle, $\theta_{TR}=50°$			
FF-α	0.45	204±70	0.39	177±61	381±93
DIR-α	0.60	491±158	0.19±0.32[c]	418±134	909±207
FF-p	0.99	449±173	1.29	586±226	1035±285
DIR-p	0.65	532±194	0.63+1.01[c]	1343±490	1875±527
ER-α	3.2[d]	775±213			775±213
ER-p	4.3[d]	1022±490			1022±490

[a]M notes particle multiplicity; σ denotes the cross section for a given reaction type (ER, FF, or DIR); the product $M\sigma$ denotes the angle-integrated cross section for particles associated with a given reaction type. The uncertainty of the particle multiplicities is estimated to be ±10% for ^{4}He and ±20% for ^{1}H.

[b]The data used here for ^{4}He are more extensive than those available in Ref. 10. They have lower thresholds and greater angular coverage. The qualitative conclusions of that study are not changed, but the multiplicity values cited should be updated by this work.

[c]The FE multiplicities for the DIR group are broken into two components: a projectilelike fragment contribution listed first, and a targetlike fragment contribution. Only the TLF contributions are considered for the calculation of the ER multiplicities.

[d]For determination of the ER multiplicities the contributions from FF and DIR were subtracted from the evaporative singles observed at back angles. See Table I for these values as well as the ER cross section. An average FF and DIR multiplicity from both trigger angles was used.

able for the composite system to emit ^{4}He, prior to scission, must necessarily be less than or near to one rotation period for the dinuclear system. For the more central collisions, leading to fissionlike breakup, one expects a larger time for more extensive particle exchanges, although this process is also expected to take place rapidly.

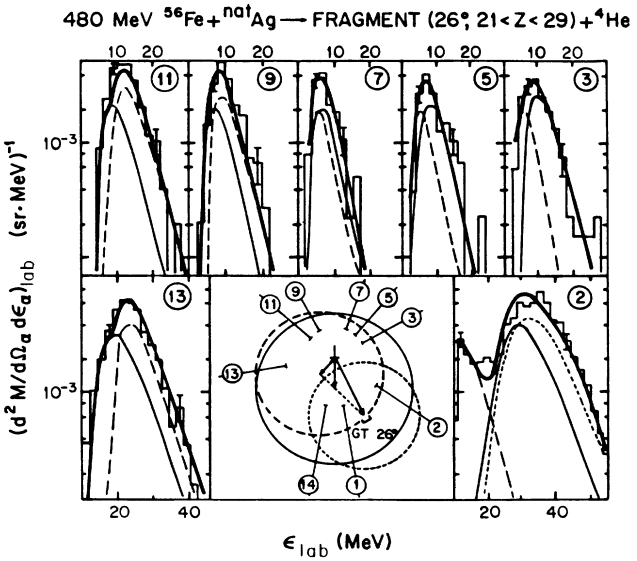

FIG. 12. Same as Fig. 10, except for DIR trigger fragments of $21 < Z < 29$, $\theta_{TR}=26°$.

Indeed, some of the very central collisions will produce evaporation residues (ER's) for which the only possibility is composite nuclear emission. It must be noted that in Figs. 10–14 a coincident fragment was required, thus eliminating the ER contribution.

What happens if we select and study those composite nuclear systems that survived for a longer period of time before scission? For this purpose we have changed the trigger angle for the fragment and measured the effect on particle multiplicity. By detecting DIR products at 50°, well beyond the grazing angle, we have required the dinuclear system to stay together longer. Figure 3 confirms that DIR products still exist at 50° even in the form of an identifiable peak in Z. Using these fragments ($21 < Z < 29$) as a coincidence gate, we obtain the spectra in Fig. 13. For this configuration detector Nos. 5, 7, and 9 emphasize CE while Nos. 2 and 13 emphasize FE. The best-fit multiplicities for the DIR gate at 50° are 0.60 for CE, 0.19 for PLF, 0.32 for TLF, and 1.11 for their sum.

The CE multiplicity has increased about twofold compared to that at 26°. We interpet this observation to mean that the amount of prescission evaporation is indeed sensitive to the lifetime of the composite system. By requiring the scission axis for the DIR fragments to rotate more extensively (50° versus 26° trigger) we have presumably excluded those events where the dinuclear system lives only briefly before the projectilelike fragment breaks away near to the grazing angle. The projectilelike fragments which were detected far away from this grazing angle must have spent longer, on average, in the dinu-

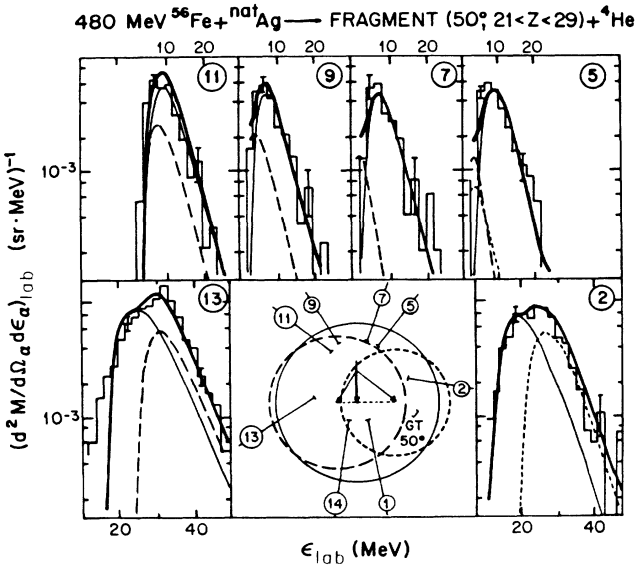

FIG. 13. Same as Fig. 10 except for DIR trigger fragments of $21 < Z < 29$, $\theta_{TR} = 50°$. In this configuration detectors 2 and 13 are located at 80° and 304° (−56°), respectively.

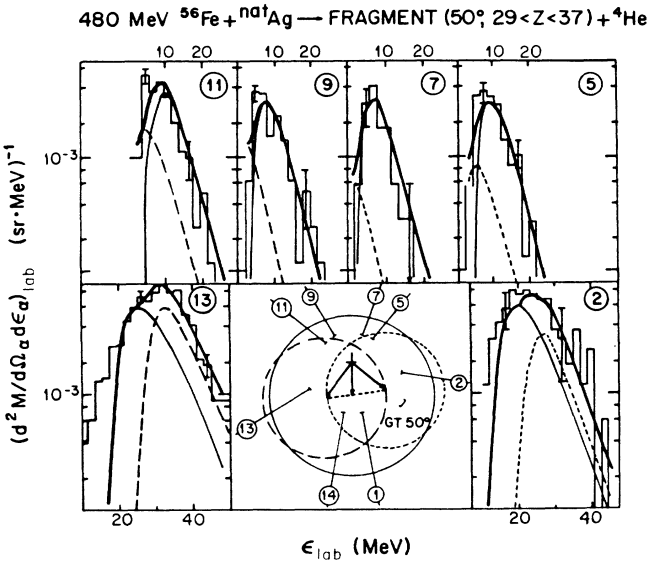

FIG. 14. Same as Figs. 10 and 13, except for FF trigger fragments of $29 < Z < 37$, $\theta_{TR} = 50°$.

clear complex before scission. The FE contributions for those coincident fragments detected at 50° are rather close to those obtained at 26°. The data for the fusion-fission-like group at 50° are also very similar to the corresponding results at 26° (see Fig. 14). The ratio is once again about 60% CE to 40% FE, and the multiplicities for the FF gate at 50° are 0.45 for CE, 0.39 for FE, and 0.84 for their sum. Therefore, it seems that the change of trigger angle (26° to 50°) has not effected any distinction of the reaction processes associated with the FF trigger (i.e., $29 < Z < 37$).

We have also recorded proton spectra (in the SST's at sideward angles) in coincidence with fragments at the same trigger angles; results for a similar analysis are shown in Figs. 15 and 16. These figures show spectra from two in-plane and two out-of-plane detectors, for each coincident fragment group. The deeply inelastic fragment trigger ($21 < Z < 29$) is on the left, and the fusion-fission-like fragment triggers ($29 < Z < 37$ and $37 < Z < 45$) are on the right. The velocity diagrams shown in Figs. 10, 11, and 12 (13 and 14) for ^{4}He are ap-

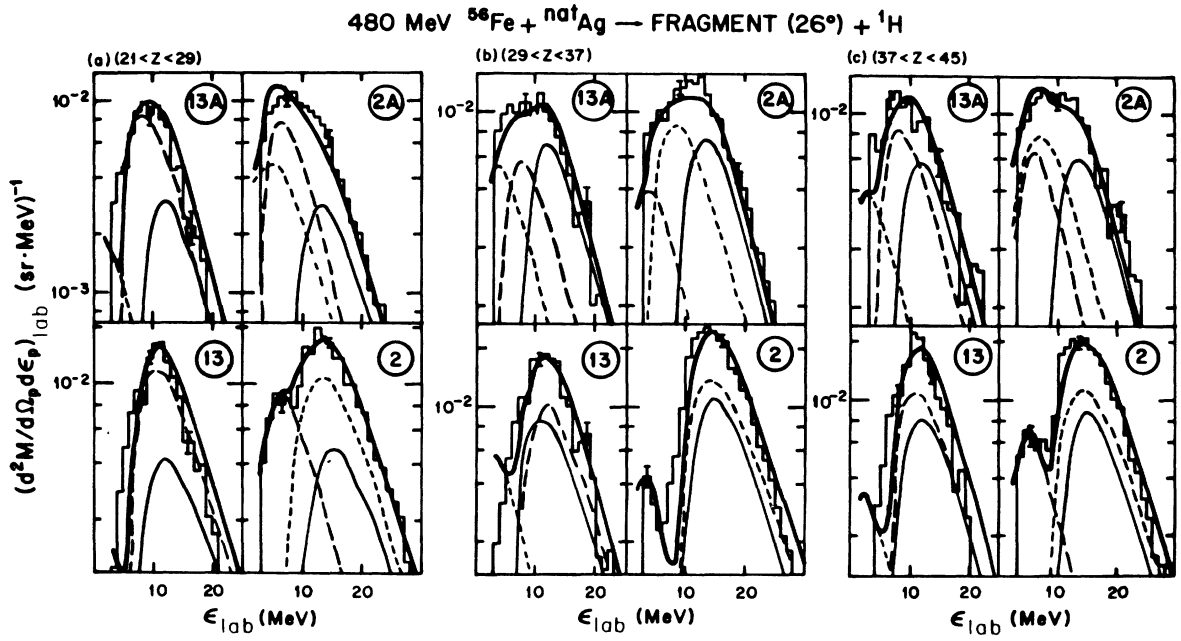

FIG. 15. Same as Fig. 10, except that these spectra are for protons in coincidence with (a) DIR fragments ($21 < Z < 29$), (b) FF fragments ($29 < Z < 37$), (c) FF fragments ($37 < Z < 45$). The fragments were detected at 26° in the lab. Note that detectors 2*A* and 13*A* are out of plane as shown in Fig. 1.

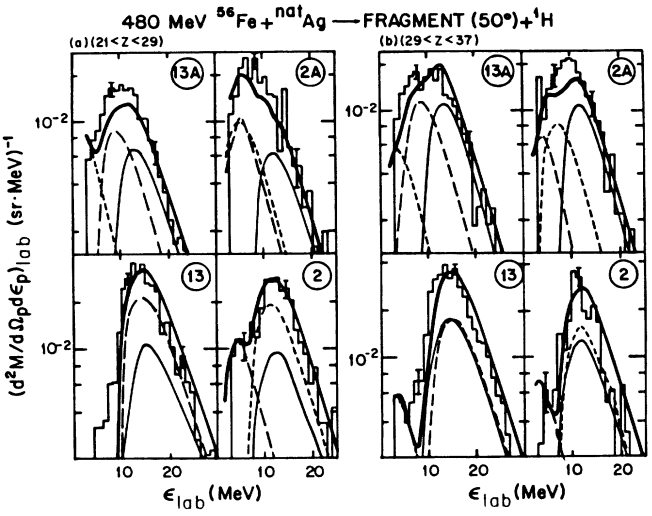

FIG. 16. Same as Fig. 10, except that these spectra are for protons in coincidence with (a) DIR ($21 < Z < 29$) and (b) FF ($29 < Z < 37$). The fragments were detected at 50° in the lab. For in-plane detector angles, see Fig. 13.

proximately the same for the ^{1}H spectra in Fig. 15 (Fig. 16). The major difference is a slightly enlarged particle velocity circle centered on each source. The low-energy "shoulder" in the experimental data for detector No. 2 gives a good point of normalization for the proton multiplicity of the undetected fragment for each coincidence gate. Next we subtract this component from the spectrum of detector No. 13, in order to fix the contribution for the composite nuclear system. Now we return to detector No. 2; by subtracting the calculated abundance of CE at this angle, we determine the ^{1}H multiplicity for the detected fragment. This procedure is simply an abbreviation of that used for ^{4}He particle coincidences; in that case there were several other detector angles that were used to verify each normalization. Accordingly, we assign a larger uncertainty for the proton multiplicities ($\approx 20\%$) than for the ^{4}He multiplicities ($< 10\%$). The resulting multiplicities are given in Table II.

There are several interesting features of the proton data. First, the DIR reactions ($\theta_{TR} = 26°$) have a lower CE multiplicity for ^{1}H than do the FF reactions. Secondly, the increase of M_{CE} for trigger angle change from 26° to 50° (for the DIR coincidences) is very similar to that observed for ^{4}He. These features for the protons confirm the notion that prescission evaporation is sensitive to the lifetime of the composite system. The major difference in the observed ^{1}H multiplicities is for the postscission evaporation. While the CE multiplities for ^{1}H and ^{4}He are very similar, the FE multiplicities are decidedly greater for ^{1}H. Approximately 60% and 80% of the protons are emitted after scission for FF and DIR reactions, respectively (for $\theta_{TR} = 26°$); for alphas these percentages are 40% and 60% for FF and DIR.

In Table II results are summarized for all the fragment-particle multiplicities, as well as those for the ER's. Note that the FF and DIR multiplicities in Table II result from the analysis detailed above. The evaporation-residue multiplicities are deduced by subtracting the cross sections for particles in coincidence with fragments from the inclusive cross sections listed in Table I. It is clear that the ER's play an important role in particle production; between 30% and 40% of the total-particle cross section arises from these most central collisions. More discussion of this subject is left for a companion paper that emphasizes the particle-particle coincidences.[35]

Figures 17 and 18 show spectra for the ^{4}He particles detected between 40° and 60° out of plane in coincidence with FF and DIR fragments. Their relative positions are

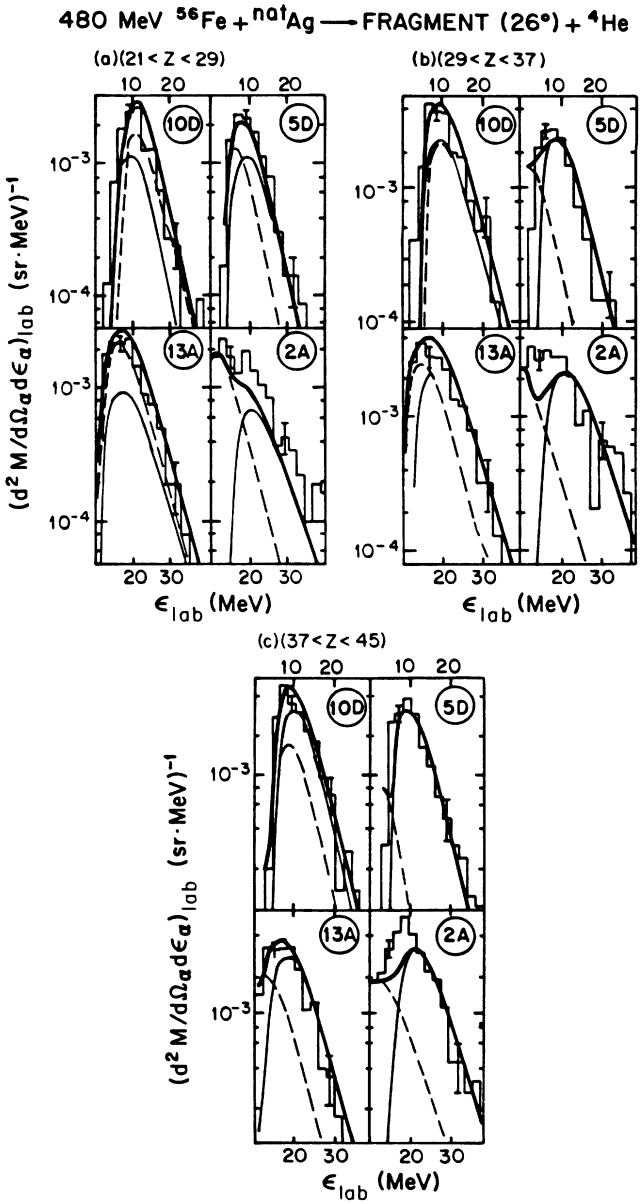

FIG. 17. Fragment-particle coincidence spectra for ^{4}He particles detected out of plane with respect to the detected fragment at 26°. The description is the same as in Fig. 10, except here the trigger fragments are (a) DIR fragments ($21 < Z < 29$), (b) FF fragments ($29 < Z < 37$), (c) FF fragments ($37 < Z < 45$). The detector positions are shown in Fig. 1.

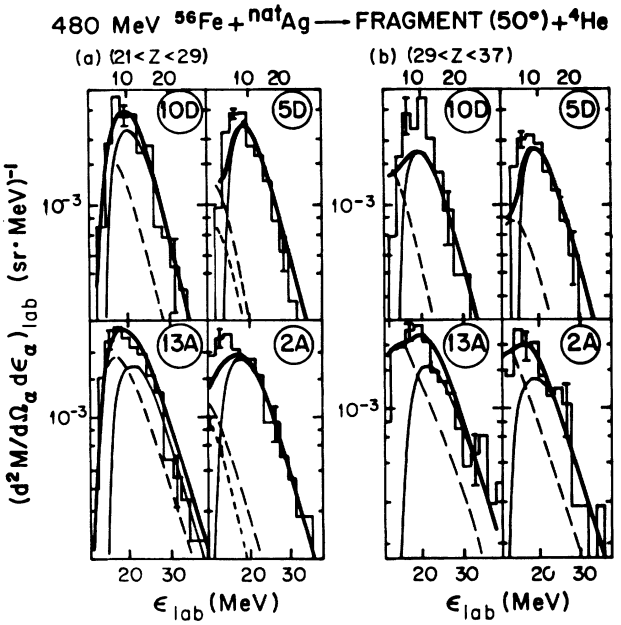

FIG. 18. Fragment-particle coincidence spectra for ^{4}He particles detected out of plane with respect to the trigger fragment at 50°. The description is the same as in Fig. 10, except here the coincident fragments are (a) DIR fragments ($21 < Z < 29$), and (b) FF fragments ($29 < Z < 37$). For in-plane detector angles, see Fig. 13.

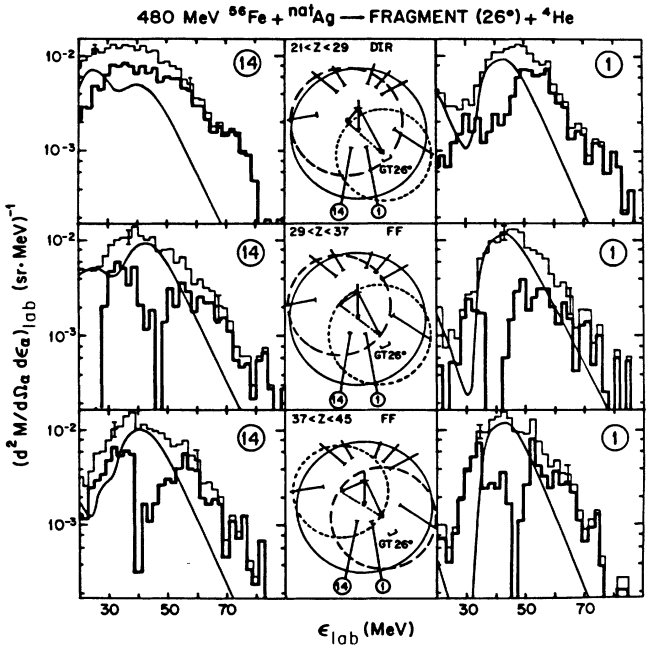

FIG. 19. Spectra of ^{4}He particles detected at $\theta_{lab} = +10°$ and $\theta_{lab} = -10°$ in coincidence with fragments at $+50°$ (light histograms). The smooth curves represent the sum of the evaporative components; their relative normalizations were determined by the other detectors. The dark histogram results from subtraction of these evaporative components from the experimental spectra.

shown in Fig. 1. Since the detection of a fragment at either 26° or 50° defines a horizontal reaction plane, these out-of-plane detectors are expected to be the most sensitive to effects of the spin of the emitters (although the in-plane angular distribution is also somewhat sensitive to spin effects). Note that, in general, the "fit" to the data is quite good for the particle spectra displayed in Figs. 10–18. For certain out-of-plane detectors, however, there is a noticeable underprediction of the cross section at low energies (e.g., detector 2*A*). These discrepancies are discussed in the next two sections.

VI. PRETHEMALIZATION EMISSION (PTE) AND NEAR-SCISSION EMISSION (NSE)

Our analysis so far has attempted to ascribe evaporative emission to one of three possible sources: a detected fragment, an undetected fragment, and the composite system prior to scission. Recently there have been many attempts to refine our understanding of these sources, as well as to identify several other sources.[11,12,16,36–39] In this reaction, we also recorded fragment-alpha-particle coincidences at 10° in the laboratory, on either side of the beam (i.e., detectors 1 and 14), and we use these detectors to demonstrate the presence of two other mechanisms for ^{4}He particle production. The data presented in Figs. 19 and 20 for which the trigger fragments were detected at 26° and 50°, respectively. Spectra for the ^{4}He in coincidence with various fragment groups are displayed along with appropriate velocity diagrams. The sum of the evaporation simulations for these angles (as determined by their normalizations at backward angles) are overlaid on the experimental histograms, and the heavy histograms result from subtraction of these evaporative components from the data.

It is clear that, after this subtraction, there is still a large amount of unaccounted-for cross section. It is in-

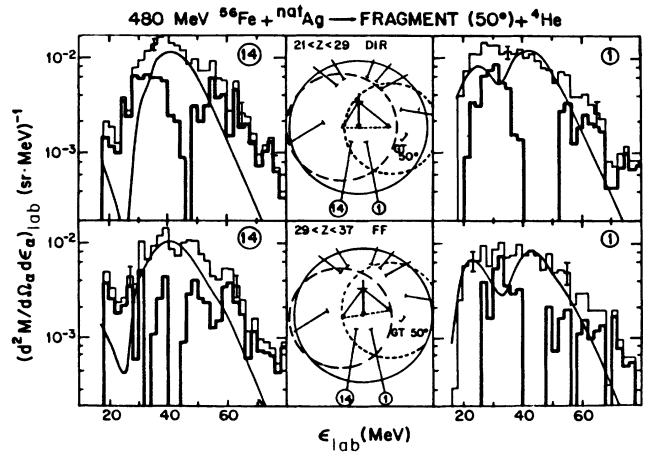

FIG. 20. Spectra of ^{4}He particles detected at $\theta_{lab} = +10°$ and $\theta_{lab} = -10°$ in coincidence with fragments at $+50°$ (light histograms). The smooth curves represent the sum of the evaporative components; their relative normalizations were determined by the other detectors. The dark histogram results from subtraction of these evaporative components from the experimental spectra.

teresting that this excess can be divided into two distinct components, at low and high energy (for all but one spectrum). We label as prethermalization emission (PTE) that portion of the unaccounted-for cross section that is centered about 60 MeV. These particles presumably arise from nonevaporative processes that involve collisions within a subset of nucleons during the early stages of the reaction. This fast PTE component is strongly forward peaked and presumably insensitive to the slower evaporative processes that follow.[3,11] The low-energy portion of the unaccounted-for cross section is centered at about 30 MeV, an energy lower than most of the evaporative components at these angles. This contribution we label as near-scission emission (NSE) because of its low energy and its angular dependence. The partial multiplicity of these types of emission (i.e., the multiplicity detected at $+10°$ and $-10°$) is given in Table III for each coincident fragment group.

In Fig. 19, in contrast to a recent report,[40] we see no left-right asymmetry for PTE. There is, however, roughly twice as much PTE in coincidence with the deeply inelastic fragment group, compared to the fusion-fission-like groups at 26°. This indicates a sensitivity of these fast particles to the entrance channel spin (and hence the impact parameter). This difference is reduced for the 50° trigger, and suggests that at this trigger angle three may not be as clear distinction of the entrance channel spin range (compared to 26°). This notion can also help explain why the 50° trigger multiplicities for the evaporative component (Table II) are so similar, regardless of the Z group of the trigger fragment.

Figure 19 does show a clear left-right asymmetry for the NSE ($\theta_{TR}=26°$). Furthermore, this asymmetry strengthens as the charge of the detected fragment decreases. For the DIR fragments the value of the ratio $[M_{NSE}(\text{left})/M_{NSE}(\text{right})]$ is about five. For the higher FF fragments, this ratio is ≈ 3.5. For the heavier FF fragments, this ratio is ≈ 1.1. This trend can be correlated with the angle with respect to the scission axis. By triggering with each fragment group, one can tilt the scission axis differently for each case. For detector 1, there is an angle of $\approx 38°$ with respect to the scission axis of an average DIR fragment ($21 < Z < 29$). For the heavier FF fragments ($37 < Z < 45$), this angle is increased to $\approx 50°$. Obviously, these NSE particles are very sensitive to the Coulomb fields of the accelerating fragments. In Fig. 20, where the trigger fragment was detected at 50°, both of the forward detectors are roughly perpendicular to the scission axis, and indeed there is no significant left-right asymmetry in the data.

TABLE III. Differential multiplicities of ^{4}He at 10° for near-scission emission (NSE) and prethermalization emission (PTE).[a,b]

Z gate		$\theta_{lab}=-10°$ NSE	$\theta_{lab}=-10°$ PTE	$\theta_{lab}=+10°$ NSE	$\theta_{lab}=+10°$ PTE
Fragment detection angle $\theta_{TR}=26°$					
$21<Z<29$	DIR:	0.058	0.069	0.012	0.062
$29<Z<37$	FF:	0.034	0.033	0.010	0.034
$37<Z<45$	FF:	0.036	0.035	0.028	0.035
Fragment detection angle, $\theta_{TR}=50°$					
$21<Z<29$	DIR:	0.099	0.077	0.084	0.043
$29<Z<37$	FF:	0.055	0.064	0.057	0.039

[a]These are partial multiplicities (i.e., multiplicities for detection at this particular angle only, not angle-integrated multiplicities). The uncertainty of the particle multiplicities is estimated to be ±10%.

[b]See Figs. 19 and 20.

These NSE particles have lower energies than expected for evaporation from a composite nucleus, and they exhibit a dependence on angle with respect to the scission axis. Hence we suggest that they are emitted near or at the time of scission of the composite system.[37,38] Since evaporative particles are observed from the composite system prior to scission and from the fully accelerated fragments after scission, it is only natural to expect a continuum of emissions extending throughout the scission process. This effect has been observed recently in other systems,[16,40] where extensive angular coverage allowed many angles for observation of this emission. The large forward velocity of the center of mass for this system precludes observation of NSE in most of the backward-angle detectors, as its average energy falls near or below the detector thresholds. However, for the out-of-plane sideward-angle detector labeled $2A$, we do see an excess of ^{4}He particles between the evaporative component from the composite system and the fragment emission at lower energy.

VII. PARAMETERS USED IN THE SIMULATION AND THEIR IMPLICATIONS

As discussed in Sec. V, the backward-angle ^{4}He spectra can be almost entirely accounted for by an appropriate combination of composite nuclear emission and fragment emission. It is important to realize that these data have not been fit at each angle independently, but rather, once the quantities of CE and FE have been determined for one detector, the simulation is fixed at all angles simultaneously. This provides very strong constraints and, therefore, gives support to the multiplicities we infer. But we must also understand that certain parameters have been adjusted in our reaction simulation in order to obtain this "best fit" to the data.

We begin our analysis by using measured-fragment cross sections to deduce the range of l values (or spin zone) associated with each trigger fragment group. As indicated in Fig. 5, the evaporation-residue cross section corresponds to an l_{ER} of approximately $64\hbar$. The fusion-fission spin zone ranges from this value of l_{ER} to an l_{crit} of approximately $110\hbar$, and the deeply inelastic reaction zone lies between l_{crit} and an l_{DIR} value of approximately $163\hbar$. These numbers have rather large uncertainties, but give reasonable bounds for the various spin zones. In GANES we use these spin ranges, along with a sharp cutoff triangular distribution, and we begin with simulated evaporation from spherical nuclei.

For fragment emission (FE), the most important parameter is the detection angle of the particle with respect

to the velocity vector of the fragment. Since we have a clear identification of fragments by their atomic number (and hence the approximate mass), and we lie well within the energy domain governed by two-body kinematics, there is very little uncertainty associated with the velocity vectors for each fragment. Even major changes in the entrance channel angular momentum (J_0) and excitation energy (E^*) have rather little effect on the final particle emission from these fragments. This is true because each fragment retains only a small fraction of the initial intrinsic spin along with a fraction of the initial excitation energy. Thus, in all our simulations of ^{4}He evaporation from the fragments (FE), we have not adjusted any parameters, and we use the default prescription given by the physics included in the program. (For details see Ref. 26).

For composite nuclear emission (CE), however, there is a great deal of sensitivity of the simulated spectra to the initial spin, excitation energy, and particle evaporation barrier.[41] As has been shown in previous studies,[3,12,42,43] if one chooses an average spherical nuclear emitter, without modifying the spin, temperature, or barrier, we cannot fit the experimental spectra. We can obtain a good fit to the data only if we adjust the properties of the composite nucleus (i.e., its emission barrier and excitation energy). For ^{4}He and ^{1}H, between 20% and 40% of the initial excitation energy must be lost, which is not surprising since GANES only considers equivalent one-step emission of particles. This fraction of the excitation energy could have been carried away by neutrons (and possibly other charged particles), or it could be tied up in deformation energy. More interesting is the difference between the observed evaporation barriers (needed to fit the in-plane data) and the empirical fusion barriers. Barrier reductions are expected, due to thermal expansion of the nuclear surface. As calculated by Chen *et al.*[44] the reductions are only several tenths of an MeV. Here, if we use a spherical emitter, we must use barriers that are $\sim$40% smaller than those for fusion; this very large reduction could suggest extensive deformation.

We have explored the possible role of nuclear deformation by modifying the GANES program to simulate evaporation from deformed nuclei. (See Ref. 41 for a complete description.) We have used Cassinian oval shapes and the nuclear Coulomb potential scheme developed by Pashkevich[46] and Carjan and Leroux.[47] Small changes were made in the Woods-Saxon nuclear potential in order to match the empirical fusion barriers between near-spherical nuclei.[45] Particle trajectories were approximated by Rutherford hyperbolas (for point charges).[19] Transmission coefficients were calculated for the particular barrier corresponding to the intersection of each hyperbola with the nuclear surface of the emitter. Orientation of the symmetry axis of the emitter nucleus was weighted according to the standard theory for fission angular distributions.[29]

In this model for evaporation from a deformed nucleus, there are two aspects of the deformation (characterized by a single Cassinian shape parameter) that cause a reduction in the energies of in-plane evaporated particles (compared to spheres). (a) The barrier seen by particles emitted from the tip of the elongated axis is reduced. (b) The moment of inertia is increased, and hence the rotational spin-off velocities are reduced. In this model the evaporation barriers are not free parameters; the spectrum of barriers is specified by the nuclear shape. Thus, only the shape parameter [or the corresponding axis ratio (b/a)] is free for adjustment.

The simulations (Figs. 10–20) for composite nuclear emitters were all calculated for heavily deformed nuclei. Only by using a Cassini deformation parameter of 0.7 to 0.8 [axis ratio (b/a) of 2.4 to 3.0] were the evaporation energies of ^{4}He and ^{1}H sufficiently reduced to produce the good fits shown. Values of the statistical-model parameters used for the composite nuclei are listed in Table IV.

We have been able to account for many of the observed features (spectral shape and angular distributions) of the light-charged particles by invoking a deformed emitter. It is instructive to note where the simulation would fail (for CE) if spherical nuclei were used. For deformed emitters, the emission barrier is greatly reduced

TABLE IV. 480 MeV ^{56}Fe + ^{nat}Ag: statistical-model parameters used for composite nuclear emitters.

	Fusion-fission-like	Deeply inelastic
$J_{rms}(\hbar)$[a]	95	147
$\tilde{\epsilon}$[b]	0.70	0.80
(b/a)[b]	2.38	3.00
$\mathcal{I}_\perp/\mathcal{I}_0$[c]	1.90	2.34
$\mathcal{I}_\parallel/\mathcal{I}_0$[c]	0.58	0.54
B^α_{max}(MeV)[d]	18.6	18.4
B^α_{min}(MeV)[d]	14.7	14.2
B^α_{fusion}(MeV)[e]	18.5	18.5
B^p_{max}(MeV)[d]	9.6	9.5
B^p_{min}(MeV)[d]	7.6	7.4
B^p_{fusion}(MeV)[e]	10.0	10.0
$\langle FEL\rangle^{\alpha}$[f]	0.2	0.2
$\langle FEL\rangle^{p}$[f]	0.4	0.4
$\tau(\alpha)$(MeV)[g]	3.2	3.0
$\tau(p)$(MeV)[g]	2.7	2.5

[a]Root-mean-square spin of the emitter.

[b]Cassini deformation parameter $\tilde{\epsilon}$ and associated axis ratio (b/a) of the deformed daughter nucleus.

[c]Moment of inertia perpendicular (parallel) to the symmetry axis compared to that of a sphere. These values are derived from the value selected for $\tilde{\epsilon}$.

[d]Barrier height for particle emission at the waist (max) or at the tips (min) of the prolate spheroid (values dependent on $\tilde{\epsilon}$). The average effective evaporation barrier is about $B_{min}+(\frac{1}{2})(B_{max}-B_{min})$, substantially smaller than B_{fusion}.

[e]Empirical fusion barriers for fusion between cold nuclei (Ref. 45), corrected for thermal expansion (Ref. 44).

[f]Fractional excitation energy lost (FEL) to particle emission (or deformation) prior to the average particle emission.

[g]Mean temperature of the daughter nucleus. These values also reflect the selected $\langle FEL\rangle$ values above.

near the long axis of the nucleus, the detection of a fragment in plane selects those reactions with spin axes perpendicular to the plane. Thus, the in-plane evaporation energies are reduced. Out-of-plane evaporation energies are enhanced as these particles are emitted predominantly near the short axis (or waist) of the deformed nucleus, where the barrier is as high or higher than for a spherical nucleus. Experimentally, as can be seen in Figs. 17 and 18 (for ^{4}He) and Figs. 15 and 16 (for ^{1}H), the high-energy, out-of-plane particles prefer the higher barriers that come from the deformed composite emitter. Also, the out-of-plane anisotropy predicted by the simulation is largely controlled by the moment of inertia and the spin of the emitter. For spherical nuclei the spin-off effect and the related out-of-plane anisotropy is much greater than actually observed.[3,12]

Is it reasonable to invoke shape distentions corresponding to more than a 2-to-1 axis ratio? Recall that we are considering only the CE process, i.e., the evaporative particles that are emitted prior to scission. We know that there is substantial CE emission, even for DIR reactions where the dinuclear system remembers its entrance channel mass asymmetry. There is also substantial particle emission from the excited fragments after scission. There is even some emission near to the time of scission. Thus, we must accept a continuum of particle evaporation times, beginning at the very earliest stages of the nuclear reaction and continuing through the deexcitation of the reaction products. Our ability to fit the data with a large static deformation may simply reflect an average deformation for a dynamic composite system enroute toward breakup. Some particles may be emitted from a compact composite system, and other from a very elongated system; the resultant evaporation spectra may possibly be best approximated by a large static deformation.

From phase-space considerations alone, it is nearly impossible to explain why so many light-charged particles are emitted prior to scission. Our data indicate that thermalization of the nuclear matter precedes the fission process and that particle evaporation is a competing process from the very beginning of the reaction. A number of other studies have also come to this conclusion.[3,6] One can use this evaporative component to study and characterize these early stages of the nuclear reaction. In fact, the dramatic change of the CE multiplicities (a factor of ≈ 2) for DIR versus FF triggers ($\theta_{TR}=26°$) suggests a method of comparing the lifetimes of dinuclear systems prior to scission in deeply inelastic reactions to that of a more completely fused system prior to fission.

VIII. CONCLUSIONS

Fragment-particle coincidence studies allow us to identify several sources of evaporated charged particles in the reaction 480 MeV ^{56}Fe + ^{nat}Ag. We find that a large number of evaporated particles (between 30% and 40%) are not in coincidence with any fragments and must, therefore, be associated with evaporation residues. For those particles that are detected in coincidence with a heavy fragment a surprisingly large percentage are evaporated prior to scission. For fusion-fission-like reactions, approximately 60% of the ^{4}He and 40% of the ^{1}H is emitted prior to scission. For deeply inelastic reactions, we find a dependence of the evaporation probability on the trigger angle of the coincident fragments. From $\theta_{TR}=26°$ (close to the grazing angle) to $\theta_{TR}=50°$ we find an increase from $\approx\frac{1}{3}$ to $\approx\frac{2}{3}$ for the prescission evaporation multiplicities of both ^{4}He and ^{1}H. At 50° (well outside the grazing angle) little difference is found between the multiplicities for fusion-fission-like and deeply inelastic-reaction events.

The observation of prescission evaporation from these high-spin systems indicates that thermalization and subsequent particle evaporation must occur very rapidly. Differences in these prescission multiplicities for reaction class (FF versus DIR) and trigger angle (26° versus 50°) suggest that this evaporation is sensitive to the lifetime of the composite emitter. This trigger-angle dependence can also explain some of the different findings reported in the literature over the years. Experimenters who have selected coincident DIR fragments near or inside the grazing angle are likely to sample much faster processes than those who trigger well outside the grazing angle. The amount of CE emission seems to be significantly smaller for this small-angle trigger.

From fits to spectral shapes and angular distributions we find that the best choice of shape for a composite nuclear emitter is one with a large deformation. In-plane barrier lowerings require large deformations [$2.4 < (b/a) < 3.0$], well beyond any reasonable saddle-point configuration for this system. The out-of-plane anisotropies and spectra support the need for a deformed composite emitter. These deformations are rationalized by considering them to be only a static representation of an ensemble of dynamically deforming systems that range from spherical to highly distended.

The combination of three evaporative sources—a detected fragment, an undetected fragment, and a composite nuclear emitter—account for most of the light particles observed in coincidence with fragments. In the forward hemisphere two additional mechanisms have been identified: prethermalization emission (PTE) and near-scission emission (NSE). More PTE is seen at 10° in coincidence with the less central DIR events (roughly twice as much for $\theta_{TR}=26°$). The NSE is found to be sensitive to the direction of the scission axis. Its center-of-mass emission velocity is well below that for composite nucleus evaporation. In summary, we have determined the principal sources of light charged particles and their mechanistic properties for the reaction 480 MeV ^{56}Fe + ^{nat}Ag.

ACKNOWLEDGMENTS

This work is based in part on the Ph.D. thesis of one of the authors (G.F.P.), Department of Chemistry, State University of New York at Stony Brook, Stony Brook, NY. This work has been supported by the Division of Nuclear Physics, Office of High Energy and Nuclear

Physics, U. S. Department of Energy. The authors wish to acknowledge the valuable support of the LBL Super-HILAC staff in providing us with reliable beam. One of us (G.P.) thanks the California State University at Fresno for the use of its facilities during part of the analysis. We also thank G. La Rana, G. Wozniak, and V. E. Viola for helpful discussions.

---

*Present address: Nuclear Science Division, Lawrence Berkeley Laboratory, Berkeley, CA 94720.

†Permanent address: Bhabha Atomic Research Centre, Nuclear Physics Division Trombay 400085, Bombay, India.

‡Permanent address: GANIL, B.P. 5027, 14021 Caen, France.

§Present address: CEN de Saclay, 91191 Gif-sur-Yvette, France.

**Permanent address: Department of Chemistry, Middle East Technical University, Ankara, Turkey.

††Permanent address: Data Systems Division, International Business Machines, Kingston, NY 12401.

[1]L. C. Vaz, D. Logan, E. Duek, J. M. Alexander, M. F. Rivet, M. S. Zisman, M. Kaplan, and J. W. Ball, Z. Phys. A **315**, 169 (1984), and references therein.

[2]M. N. Namboodiri, R. K. Choudhury, L. Adler, J. D. Bronson, D. Fabris, U. Garg, P. L. Gonthier, K. Hagel, D. R. Haenni, Y. W. Lui, Z. Majka, G. Mouchaty, T. Murakami, J. B. Natowitz, G. Nebbia, R. P. Schmitt, S. Simon, J. P. Sullivan, and D. H. Youngblood, Phys. Rev. C **35**, 149 (1987), and references therein.

[3]R. A. Lacey, N. N. Ajitanand, J. M. Alexander, D. M. de Castro Rizzo, G. F. Peaslee, L. C. Vaz, M. Kaplan, M. Kildir, G. La Rana, D. J. Moses, W. E. Parker, D. Logan, M. S. Zisman, P. DeYoung, and L. Kowalski, Phys. Rev. C **37**, 2540 (1988), and references therein, **37**, 2561 (1988), and references therein.

[4]R. Babinet, B. Cauvin, J. Girard, J. M. Alexander, T. H. Chiang, J. Galin, B. Gatty, D. Guerreau, and X. Tarrago, Z. Phys. A **295**, 153 (1980).

[5]L. G. Sobotka, R. J. McDonald, G. J. Wozniak, D. J. Morrissey, A. J. Pacheco, and L. G. Moretto, Phys. Rev. C **28**, 219 (1983), and references therein.

[6]D. J. Moses, M. Kaplan, M. Kildir, D. R. G. Logan, G. La Rana, W. E. Parker, R. Lacey, G. F. Peaslee, J. M. Alexander, N. N. Ajitanand, L. C. Vaz, and M. S. Zisman, Nucl. Phys. **A465**, 339 (1987), and references therein.

[7]D. Logan, M. Rajagopalan, M. S. Zisman, J. M. Alexander, M. Kaplan, and L. Kowalski, Phys. Rev. C **22**, 104 (1980).

[8]M. F. Rivet, B. Gatty, H. Guillemot, B. Borderie, R. Bimbot, I. Forest, J. Galin, D. Gardes, D. Guerreau, M. Lefort, X. Tarrago, B. Tamain, and L. Novicki, Z. Phys. A **307**, 365 (1982).

[9]S. Song, M. F. Rivet, R. Bimbot, B. Borderie, I. Forest, J. Galin, D. Gardes, B. Gatty, M. Lefort, H. Oeschler, B. Tamain, and X. Tarrago, Phys. Lett. **130B**, 14 (1983).

[10]N. N. Ajitanand, J. M. Alexander, H. Delagrange, E. Duek, D. O. Eriksen, D. Guerreau, M. Kaplan, M. Kildir, L. Kowalski, R. Lacey, D. Logan, D. J. Moses, G. F. Peaslee, L. C. Vaz, and M. S. Zisman, Z. Phys. A **316**, 169 (1984).

[11]E. Duek, N. N. Ajitanand, J. M. Alexander, D. Logan, M. Kildir, L. Kowalski, L. C. Vaz, D. Guerreau, M. S. Zisman, M. Kaplan, and D. J. Moses, Z. Phys. A **317**, 83 (1984).

[12]L. Schad, H. Ho, G.-Y. Fan, B. Lindl, A. Pfoh, R. Wolski, and J. P. Wurm, Z. Phys. A **318**, 179 (1984).

[13]D. J. Hinde, R. J. Charity, G. S. Foote, J. R. Leigh, J. O. Newton, S. Ogaza, and A. Chattejee, Nucl. Phys. **A452**, 550 (1986).

[14]D. Hilscher, D. J. Hinde, and H. Rossner, in *Proceedings of the Conference on Hot Nuclei, College Station, Texas,* edited by R. P. Schmitt, S. Schlomo, and J. B. Natowitz (Academic, NY, in press).

[15]A. Gavron, A. Gayer, J. Boissevain, H. C. Britt, T. C. Awes, J. R. Beene, B. Cheynis, D. Drain, R. L. Ferguson, F. E. Obenshain, F. Plasil, G. R. Young, G. A. Petitt, and C. Butler, Phys. Rev. C **35**, 579 (1987).

[16]B. Lindl, A. Brucker, M. Bantel, H. Ho, R. Muffler, L. Schad, M. G. Trauth, and J. P. Wurm, Z. Phys. A **328**, 85 (1987).

[17]G. J. Wozniak, G. J. Mathews, R. P. Schmidt, R. Regimbart, H. Hubel, R. M. Diamond, and L. G. Moretto, Nucl. Phys. **A402**, 332 (1983).

[18]T. Ericson, Adv. Phys. **9**, 423 (1960), and references therein.

[19]T. Dossing, Licentiat Thesis, University of Copenhagen, Denmark, 1977, and references therein.

[20]G. F. Peaslee, Ph.D. dissertation, Dept. of Chemistry, State University of New York at Stony Brook, 1988.

[21]M. M. Fowler and R. C. Jared, Nucl. Instrum. Methods **124**, 341 (1975).

[22]D. J. Moses, Ph.D. dissertation, Dept. of Chemistry, Carnegie-Mellon University, 1986.

[23]S. B. Kaufman, E. P. Steinberg, B. D. Wilkins, J. Unik, A. J. Gorski, and M. J. Fluss, Nucl. Instrum. Methods **115**, 47 (1974).

[24]T. W. Armstrong and K. C. Chandler, Oak Ridge National Laboratory Internal Report No. (Mathematics Division) ORNL-4869, 1973 (unpublished).

[25]K. Lutzenkirchen, J. V. Kratz, G. Wirth, W. Bruchle, L. Dorr, K. Summerer, R. Lucas, J. Poitou, C. Gregoire, and S. Bjornholm, Z. Phys. A **320**, 529 (1985), and references therein.

[26]N. N. Ajitanand, R. Lacey, G. F. Peaslee, E. Duek, and J. M. Alexander, Nucl. Instrum. Methods A **243**, 111 (1986).

[27]B. Sikora, W. Scobel, M. Beckerman, J. Bisplinghoff, and M. Blann, Phys. Rev. C **25**, 1446 (1982).

[28]M. Blann, D. Akers, T. A. Komoto, F. S. Dietrich, L. F. Hansen, J. G. Woodworth, W. Scobel, J. Bisplinghoff, B. Sikora, F. Plasil, and R. L. Ferguson, Phys. Rev. C **26**, 1471 (1982).

[29]L. C. Vaz and J. M. Alexander, Phys. Rep. **97C**, 1 (1983).

[30]W. W. Wilcke, J. R. Birkelund, H. J. Wollensheim, A. D. Hoover, J. R. Huizenga, W. U. Schröder, and L. E. Tubbs, At. Data Nucl. Data Tables **25**, 389 (1980).

[31]J. M. Alexander, Ann. Phys. (Paris) **12**, 603 (1987).

[32]V. E. Viola, Jr., Nucl. Data **1**, 39 (1966); V. E. Viola, K. Kwiatkowski, and M. Walker, Phys. Rev. C **31**, 1550 (1985).

[33]I. Halpern and V. M. Strutinski, in *Proceedings of the Second United Nations Conference on the Peaceful Uses of Atomic Energy* (United Nations, Geneva, Switzerland, 1958), Vol. 15, p. 408.

[34]R. Vandenbosch and J. R. Huizenga, *Nuclear Fission* (Academic, London, 1973).

[35]G. F. Peaslee, N. N. Ajitanand, J. M. Alexander, R. Lacey, L. C. Vaz, M. Kaplan, M. Kildir, D.J. Moses, D. Logan, M. S.

Zisman, and L. Kowalski (submitted to Phys. Rev. C).
[36]G.-Y. Fan, H. Ho, P. L. Gonthier, W. Kuhn, A. Pfoh, L. Schad, R. Wolski, J. P. Wurm, J. C. Adloff, D. Disdier, V. Rauch, and F. Scheibling, Z. Phys. A **310**, 269 (1983).
[37]E. Duek, N. N. Ajitanand, J. M. Alexander, D. Logan, M. Kildir, L. Kowalski, L. C. Vaz, D. Guerreau, M. S. Zisman, and M. Kaplan, Phys. Lett. **131B**, 297 (1983).
[38]M. Kaplan, M. Kildir, N. N. Ajitanand, J. M. Alexander, and E. Duek, Phys. Rev. Lett. **51**, 1492 (1983).
[39]D. J. Hinde, R. J. Charity, G. S. Foote, J. R. Leigh, J. O. Newton, S. Ogaza, and A. Chatterjee, Phys. Rev. Lett. **52**, 986 (1984); **53(E)**, 2275 (1984).
[40]A. Brucker, B. Lindl, M. Bantel, H. Ho, R. Muffler, L. Schad, M. G. Trauth, and J. P. Wurm, Phys. Lett. **186B**, 20 (1987).
[41]N. N. Ajitanand, G. La Rana, R. Lacey, D. J. Moses, L. C. Vaz, G. F. Peaslee, D. M. de Castro Rizzo, M. Kaplan, and J. M. Alexander, Phys. Rev. C **34**, 877 (1986).
[42]D. J. Moses, M. Kaplan, G. La Rana, W. E. Parker, R. Lacey, and J. M. Alexander, Phys. Rev. C **36**, 422 (1987).
[43]G. La Rana, D. J. Moses, W. E. Parker, M. Kaplan, D. Logan, R. Lacey, J. M. Alexander, and R. J. Welberry, Phys. Rev. C **35**, 373 (1987).
[44]X. S. Chen, C. Ngo, and E. Thomasi, M. Barranco, X. Vinas, and H. Ngo, Nucl. Phys. **A401**, 143 (1983).
[45]L. C. Vaz and J. M. Alexander, Z. Phys. **318**, 231 (1984).
[46]V. V. Pashkevich, Nucl. Phys. **A169**, 275 (1971).
[47]N. Carjan and B. Leroux, Phys. Rev. C **22**, 2008 (1980).